Nuclear magnetic resonance reveals a two hairpin equilibrium near the 3′-splice site of influenza A segment 7 mRNA that can be shifted by oligonucleotides

ANDREW D. KAUFFMANN,[1,2] SCOTT D. KENNEDY,[3] WALTER N. MOSS,[4] ELZBIETA KIERZEK,[5] RYSZARD KIERZEK,[5] and DOUGLAS H. TURNER[1,2]

[1]Department of Chemistry, University of Rochester, Rochester, New York 14627, USA
[2]Center for RNA Biology, University of Rochester, Rochester, New York 14627, USA
[3]Department of Biochemistry and Biophysics, University of Rochester School of Medicine and Dentistry, Rochester, New York 14642, USA
[4]Department of Biochemistry, Biophysics, and Molecular Biology, Iowa State University, Ames, Iowa 50011, USA
[5]Institute of Bioorganic Chemistry, Polish Academy of Sciences, 61-704 Poznan, Poland

ABSTRACT

Influenza A kills hundreds of thousands of people globally every year and has the potential to generate more severe pandemics. Influenza A's RNA genome and transcriptome provide many potential therapeutic targets. Here, nuclear magnetic resonance (NMR) experiments suggest that one such target could be a hairpin loop of 8 nucleotides in a pseudoknot that sequesters a 3′ splice site in canonical pairs until a conformational change releases it into a dynamic 2 × 2-nt internal loop. NMR experiments reveal that the hairpin loop is dynamic and able to bind oligonucleotides as short as pentamers. A 3D NMR structure of the complex contains 4 and likely 5 bp between pentamer and loop. Moreover, a hairpin sequence was discovered that mimics the equilibrium of the influenza hairpin between its structure in the pseudoknot and upon release of the splice site. Oligonucleotide binding shifts the equilibrium completely to the hairpin secondary structure required for pseudoknot folding. The results suggest this hairpin can be used to screen for compounds that stabilize the pseudoknot and potentially reduce splicing.

Keywords: influenza; splicing; hairpin target; oligonucleotide; NMR

INTRODUCTION

Influenza A virus (IAV) continues to cause yearly epidemics that typically kill hundreds of thousands of people globally and tens of thousands in the United States (Salomon and Webster 2009; Biggerstaff et al. 2018; Putri et al. 2018). The United States Centers for Disease Control and Prevention scores flu seasons on the basis of visits to outpatient clinics, influenza-associated hospitalizations, and deaths (Biggerstaff et al. 2018). In this century, high severity has been assigned to the 2003–2004, 2014–2015, and 2017–2018 seasons, even though seasonal vaccines are available. Currently, only limited relief is available from small molecule therapeutics such as oseltamivir (Tamiflu), amantadine, and baloxavir marboxil (XOFLUZA) (Min and Subbarao 2010; Sheu et al. 2011; Hayden et al. 2018). All inhibit proteins and are susceptible to the development of resistance (Gubareva et al. 2019; Takashita et al. 2019). Several preclinical studies have tested oligonucleotide approaches that typically use sequences between 15 (Pao et al. 2014) and 42 (Hoy 2018) nucleotides (Lenartowicz et al. 2016; Michalak et al. 2019; Dhuri et al. 2020; Szabat et al. 2020). On the basis of NMR structural studies of small model hairpins, we suggest the possibility that short oligonucleotides or small molecules could be used to shift an RNA dynamic equilibrium to inhibit splicing and viral propagation.

Bioinformatics studies on IAV revealed several areas of evolutionarily conserved RNA secondary structures (Gultyaev et al. 2007; Ilyinskii et al. 2009; Moss et al. 2011; Moss and Steitz 2015; Soszynska-Jozwiak et al. 2015; Kobayashi et al. 2016). Because these structures have been preserved during evolution, it is likely that they accomplish a

Corresponding author: turner@chem.rochester.edu
Article is online at http://www.rnajournal.org/cgi/doi/10.1261/rna.078951.121.

function beneficial for viral viability, thus making them attractive therapeutic targets. RNA structure can have a role in regulating splicing (Warf and Berglund 2010). One of the conserved regions contains the 3′ splice site of IAV segment 7 mRNA (Moss et al. 2011). This sequence is predicted to exist in a structural equilibrium between a pseudoknot and a long hairpin (Fig. 1A). NMR spectra show that in the hairpin stem (S7HP in Fig. 1A), the splice site is exposed in a dynamic internal loop (Chen et al. 2015). Within the predicted pseudoknot, however, the splice site is sequestered in a helix (S7PK in Fig. 1A). Chemical mapping and gel shift assays in solution confirmed the equilibrium between two conformations and showed that this equilibrium is affected by Mg^{2+} and $[Co(NH_3)_6]^{3+}$ concentration (Moss et al. 2012). If conservative rules for interpreting DMS mapping are used (Mathews et al. 2004), then DMS mapping in cell culture (Simon et al. 2019) is consistent with the presence of predicted structures, assuming that the GU and three AU pairs at the 3′ termini (Fig. 1A) are dynamic. A mutational study showed that disrupting this structural equilibrium to favor retainment of the splice site in a helix increased production of unspliced mRNA and decreased viral viability in cell culture (Jiang et al. 2016). We speculate that the structural equilibrium could provide an on/off switch for regulating splicing.

Because the protein products and temporal expression of unspliced (M1) and spliced (M2) segment 7 mRNA are essential to the virus (Martin and Helenius 1991; Pinto et al. 1992; Holsinger et al. 1994; Shih et al. 1995; Pielak and Chou 2011), the proposed conformational on/off switch for splicing poses a potentially attractive target for therapeutics. Although most therapeutics target proteins, RNA is increasingly investigated as a drug target (Angelbello et al. 2018; Warner et al. 2018; Bennett et al. 2019; Meyer et al. 2020; Sreeramulu et al. 2021), including at splice sites (Dominski and Kole 1993; Goemans et al. 2011; Voit et al. 2014) and pseudoknots (Rangan et al. 2021; Sreeramulu et al. 2021). Significantly, even short hairpins appear to be promising targets for therapeutics (Davila-Calderon et al. 2020; Haniff et al. 2020; Lulla et al. 2021). Oligonucleotide-based therapeutics can be easily designed to target a specific RNA sequence due to base-pairing properties of nucleic acids (Watt et al. 2020).

Herein, we present NMR studies of two 19-nt hairpins (Fig. 1), 5′GUCCAGAAACGGAUGGACA (HP1) and 5′AU CCAGAAACGGAUGGAUA (HP2), derived from the consensus sequence of IAV segment 7 mRNA nucleotides 720–733 (Moss et al. 2011). To increase folding stability, 2 bp were added to the wild-type sequence, a UA in both hairpins and a GC in HP1 and an AU in HP2. NMR spectra of HP1 reveal a dynamic 8-nt hairpin loop. Similar to the natural sequence, HP2 is in equilibrium between two secondary structures. Three oligonucleotides complementary to the 8-nt hairpin loop of S7PK (Fig. 1A) shift this equilibrium to the base-pairing expected to stabilize the 8-nt hairpin of the native pseudoknot, as modeled by HP2-PK (Fig. 1C). Thus, HP2 could provide a simple target to screen for compounds that could stabilize the pseudoknot. Such

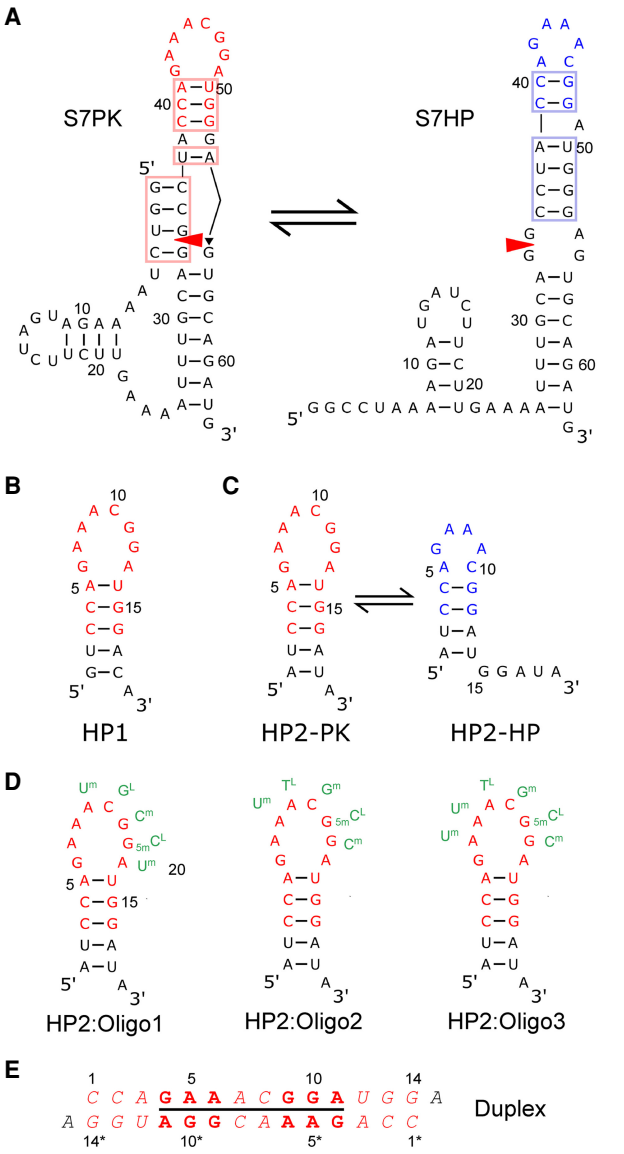

FIGURE 1. (*A*) Conserved region of influenza A segment 7 mRNA showing the 3′ splice site (red triangle) in two secondary structures predicted from sequence comparison (Table 1): a pseudoknot with hidden splice site (S7PK) and a long hairpin with exposed splice site (S7HP). Colored nucleotides are included in model hairpins shown in *B*–*D*. Colored boxes correlate with colors highlighting base pairs in Table 1. (*B*,*C*) Two 19-nt hairpins, HP1 and HP2, used for NMR studies. HP1 (*B*) and HP2 (*C*) shown in two hairpin loop conformations corresponding to those predicted in pseudoknot (HP2-PK) and hairpin (HP2-HP) of segment 7 mRNA. (*D*) HP2 with Oligonucleotides 1, 2, and 3 designed to target the loop as shown. The 5′ end of each oligonucleotide is assigned number 20. In the oligonucleotide residue names, "L" is LNA, "m" is 2′-O-methyl in the sugar, and "5m" is 5-methyl in the base. T^L is thymidine LNA. (*E*) Self-complementary duplex with 8 × 8-nt internal loop formed by 5′CCAGAAACGGAUGGA at 100 mM K^+ (Kauffmann et al. 2017).

compounds could be used to test the pseudoknot/hairpin hypothesis for splicing regulation and potentially provide lead therapeutics.

RESULTS

Sequence design and buffer conditions

The pseudoknot/hairpin splicing hypothesis was originally generated from sequence comparisons of base-pairing and predicted thermodynamic stabilities for roughly 500 IAV sequences (Moss et al. 2011). Sequence comparisons of base-pairing (Tables 1, 2; Figs. 1, 2) were extended to over 22,000 sequences from the influenza virus resource at the National Center for Biotechnology Information (Bao et al. 2008). Except for the C39–G48 base pair in the S7HP hairpin stem, all other base pair positions in S7PK and S7HP secondary structures (Table 1; Figs. 1, 2) are conserved with canonical pairs in more than 89% of sequences. This includes the C39–G52 base pair in S7PK. The C39–G48 base pair in S7HP is CG, CA, UA, and UG, respectively, in 41%, 31%, 23%, and 5% of sequences. These mutations likely allow similar 2 and 3D structures, but with a variety of possibilities for the bulged nucleotide. A49 is 100% conserved and not canonically base-paired in the S7HP secondary structures shown in Figures 1 and 2 (Chen et al. 2015). However, A49 is able to form a G42A49 pair in S7PK (Table 2; Figs. 1, 2). On the basis of base fractions in Table 2, G22A7 and/or G63A25 are also able to form GA pairs. GA pairs capping helixes are common in RNA (Elgavish et al. 2001) and are thermodynamically stabilizing (Sugimoto et al. 1987).

To study the hairpin, a common natural sequence, CCAGAAACGGAUGGA, was originally used with the 3′ dangling A for added stability. However, in buffer containing 80 mM KCl, 20 mM potassium phosphate, and 0.05 mM Na_2EDTA (pH 6.2), the natural sequence forms a self-complementary duplex consisting of an 8 × 8-nt internal loop (Kauffmann et al. 2017). Duplex was the majority stoichiometry even at 15 µM RNA. Screening of various sequences and conditions led to discovery that HP1 and HP2 (Fig. 1B,C) form only hairpins in, respectively, 2.0 and 10.0 mM potassium phosphate with 0.05 mM Na_2EDTA (pH 6.2). Both have a longer stem to stabilize the hairpin in low salt.

HP1 forms a hairpin with a dynamic loop

One-dimensional imino proton spectra at both 1.5 mM and 35 µM RNA along with 2D NOESY spectra at 1.5 mM RNA (Fig. 3; Supplemental Figs. S1, S2) show that HP1 has the secondary structure in Figure 1B. Although the hairpin forms a stable, singular secondary structure, the 8-nt hairpin loop is dynamic. This differs from the self-complementary duplex, $(5'CCAGAAACGGAUGGA)_2$, at 100 mM K^+ (Fig. 1E; Kauffmann et al. 2017). The underlined internal loop of the duplex has two copies of the same loop sequence as HP1, but forms two stable 3RRs motifs (Lerman et al. 2011) with each containing three sheared GA (*trans* Hoogsteen/sugar edge) pairs (Kauffmann et al. 2017). Despite the dynamics, NMR spectra provide insight into features of the HP1 loop.

In HP1, nucleobases A7, A8, and A13 are intrahelical, but do not form stable GA pairs

Table 3 contains comparisons of NOE distances and chemical shifts for HP1 and the duplex. Clearly, the loop conformations are quite different. For example, the A13P chemical shift of −2.6 ppm for HP1 is slightly downfield from the HP1 and duplex average range of −4.0 ppm ± 0.4 ppm. In contrast, the equivalent shift of A11/11*P in the duplex is 0.2 ppm due to the distorted backbone between adjacent sheared GA pairs. The shift of 4.6 ppm for G11H2′ in HP1 is within the HP1 and duplex average range of 4.5 ppm ± 0.2 ppm. In contrast, the equivalent shift for G9/9* in the duplex is 3.4 ppm due to positioning over the ring of G10/10* (Kauffmann et al. 2017). Additionally, the imino proton resonances in HP1 for G6, G11, and G12 are very broad and have no detectable cross-peaks (Fig. 3A; Supplemental Fig. S1), which is in contrast to spectra for duplex (Kauffmann et al. 2017). Although the data do not eliminate the possibility of GA pairs, they do suggest that if sheared GAs form they are likely transient and allow exchange of the loop G imino protons with water. Evidently, the HP1 hairpin loop populates an ensemble of conformations. Nevertheless, the NOEs (Table 3) place A7, A8, and A13 of HP1 inside the loop. The A8H2 to G11H2′ NOE of 3.2 Å implies that the backbone makes a 180° turn between A8 and G11.

The chemical shift and NOE data suggest possible similarities in addition to the differences described above between HP1 and the 3RRs motif in the duplex. The A13P and U14H1′ chemical shifts in HP1 are the only ^{31}P and H1′ that are shifted in the same direction as the unique ^{31}P and H1′ in the equivalent residues of duplex (A11/11* and U12/12*, respectively) (see Table 3; Supplemental Table S1; Supplemental Fig. S3). These shifts suggest that A13 and U14 in HP1 may spend time in a sheared GA/Watson–Crick AU conformation similar to A11/11* and U12/12* in duplex. As described below, G6 is primarily *anti* relative to its ribose, and its ribose has primarily C3′-endo pucker. Both characteristics are also consistent with partial pairing to A13.

In the HP1 loop, G11 and G12 spend roughly half their time in the *syn* glycosidic torsion conformation

NMR provides additional evidence for a dynamic HP1 loop. The $^{13}C8$ chemical shifts of G11 and G12 (139.81 and 140.14 ppm, respectively) are ∼3 ppm downfield

TABLE 1. Base pair (i–j) counts for S7PK and S7HP[a,b]

i	j	GC	CG	AU	UA	GU	UG	GA	AG	AA	GG	UU	CC	AC	UC	CA	CU	%Canonical
1	36	20765	0	0	0	1279	0	681	0	1	11	0	12	3	0	0	0	96.8
2	35	22722	0	0	0	24	0	7	0	0	7	0	0	2	1	0	0	99.9
3	34	0	246	0	3751	0	18686	1	28	2	30	0	0	0	1	12	0	99.6
4	33	0	22167	0	0	0	548	0	9	0	5	0	0	0	0	1	1	99.8
8	21	8	0	16024	0	6638	0	0	0	0	0	0	0	91	0	0	0	99.6
9	20	0	0	21635	0	1122	0	0	0	0	0	0	0	0	0	0	0	100.0
10	19	20332	0	1	0	1	0	1737	0	0	0	0	1	692	0	0	0	89.3
11	18	2	0	21633	0	5	0	0	9	7	0	1	0	1106	0	0	0	95.1
26	62	0	0	22757	0	1	0	0	0	0	0	3	0	2	0	0	2	100.0
27	61	0	0	0	21195	0	21	0	0	16	0	13	4	1	1133	375	0	93.2
28	60	0	12	0	8750	0	13878	0	0	0	1	2	0	0	2	111	0	99.5
29	59	0	0	0	22758	0	0	4	0	0	0	0	0	0	1	1	0	100.0
30	58	20418	0	0	0	0	0	0	0	0	0	0	0	2338	1	0	0	89.7
31	57	0	22643	0	0	0	0	0	0	0	0	0	4	0	0	106	10	99.5
32	56	0	0	22758	0	0	0	0	4	0	0	1	0	2	0	0	0	100.0
33	*55*	*3*	*0*	*0*	*0*	*240*	*0*	*34*	*1*	*0*	*22484*	*0*	*0*	*0*	*1*	*0*	*0*	*1.1*
34	*54*	*16*	*0*	*4*	*0*	*192*	*0*	*17230*	*3482*	*279*	*1545*	*0*	*0*	*1*	*0*	*1*	*0*	*0.9*
35	53	0	22725	0	0	0	24	0	7	0	7	0	0	0	0	1	0	99.9
36	52	0	20781	0	0	0	1279	0	682	0	11	0	0	0	0	0	0	96.9
37	51	0	5	0	0	0	22755	0	0	0	0	2	0	0	0	0	0	100.0
37	54	0	0	0	17504	0	5031	0	0	0	0	196	0	0	17	5	0	99.0
38	50	0	0	22740	0	0	0	0	4	3	0	14	0	0	0	0	0	99.9
39	48	0	9349	0	5144	0	1144	0	0	0	0	1	7	0	2	7089	14	68.7
40	47	0	22760	0	0	0	0	0	0	0	0	0	2	0	0	1	0	100.0
39	52	0	16467	0	0	0	6291	0	0	0	0	0	0	0	0	0	0	100.0
40	51	0	22763	0	0	0	0	0	0	0	0	0	0	0	0	0	2	100.0
41	50	0	0	22750	0	1	0	0	4	3	0	1	0	0	0	0	1	99.9
41	*46*	*1*	*0*	*3*	*0*	*0*	*0*	*0*	*0*	*346*	*0*	*0*	*1*	*22408*	*1*	*0*	*0*	*0.0*

[a]Canonical and noncanonical pairs are tabulated to the left and right, respectively.
[b]Shaded red pairs in left column are only in S7PK. Blue pairs are only in S7HP. Counts shaded gray are >95% of one base pair type.

compared with other guanosine residues in HP1 and duplex at 137.1 ppm ± 1.0 ppm (Table 3). A downfield shift of ^{13}C8 is predicted and observed in *syn* guanosine residues. Additionally, for G11 and G12, NOE distances between H8 and its own H1′ (2.9 and 2.8 Å, respectively) (Table 3) are shorter than expected for the *anti* conformation (3.5 Å ± 0.1 Å in stem of HP1), but longer than expected for pure *syn* residues (2.5 Å ± 0.1 Å). This chemical shift and NOE data suggest that close to 50% of G11 and G12 residues are in the *syn* conformation. G6 appears to be primarily *anti*, based on a ^{13}C8 chemical shift of 138.01 ppm (Supplemental Table S1) and G6H8-H1′ NOE distance of 3.30 Å (Table 3).

A7 to A13 ribose groups in HP1 are dynamic

A TOCSY spectrum (Fig. 4) reveals that sugars for G6 to G12 in the HP1 loop are dynamic with at least partial C2′-endo ribose pucker. In a 400 msec mixing time NOESY spectrum, H1′–H2′ cross-peaks showed scalar-couplings measured from peak splitting to range between 3.0 Hz for G6, A7, A8, and 6.1 Hz for C10 (Fig. 4). The 3.0 and 6.1 Hz splittings, respectively, suggest preferences for C3′-endo and C2′-endo ribose puckers. Additionally, these seven residues had C1′ upfield chemical shifts compared with the other residues (Supplemental Table S1). The TOCSY spectrum had almost no H1′–H2′ cross-peak for A13, consistent with C3′-endo ribose pucker. The A13H1′ peak is broad, however, which may be a result of small H1′–H2′ coupling or conformational dynamics, or both.

HP2 has two secondary structures in equilibrium

The 1D NMR spectrum of HP2 at 1°C has eight definite imino proton resonances consistent with Watson–Crick pairs (Fig. 3B). Two-dimensional NMR spectra reveal two secondary structures in slow exchange as indicated by large exchange cross-peaks near the diagonal in the aromatic region of the TOCSY spectrum (Fig. 5). The two secondary structures were determined to be HP2-PK and HP2-HP (Fig. 1C). Based on relative intensities of corresponding imino proton resonances in two samples at 1°C, roughly 64 ± 8% of the RNA folds into HP2-PK, with the rest forming HP2-HP. Thermodynamic parameters for 1 M NaCl (Turner and Mathews 2010) in the RNAstructure program (Mathews 2014) predict the equilibrium, though with a higher fraction of HP2-PK. Higher salt is expected to favor the structure with higher charge density (Manning 1978), and stabilization by more than one 3′-terminal dangling end is not included in the thermodynamic model.

Comparison of chemical shifts between HP2-PK and HP1 indicate that 3D structures of these hairpin loops are

TABLE 2. Nucleotide fractions for S7PK and S7HP

Pos:	1	2	3	4	5	6	7	8	9	10	11	12	13	14	15	16	17	18
A	0.02	0.01	0.13	0.04	0.01	40.60	100.00	70.80	95.07	3.04	99.96	0.11	8.17	99.98	0.00	0.0	0.00	0.03
G	99.93	99.99	0.14	0.02	0.00	59.13	0.00	29.20	4.93	96.95	0.03	0.00	91.83	0.00	0.00	0.0	0.00	0.04
C	0.05	0.00	1.13	97.53	0.01	0.04	0.00	0.00	0.00	0.00	0.00	1.26	0.00	0.01	26.49	99.9	0.01	4.87
U	0.00	0.00	98.60	2.41	99.98	0.22	0.00	0.00	0.00	0.00	0.00	98.62	0.00	0.00	73.51	0.0	99.99	95.06
-	0.00	0.00	0.00	0.00	0.00	0.00	0.00	0.00	0.00	0.00	0.00	0.00	0.00	0.00	0.00	0.0	0.00	0.00
Pos:	**19**	**20**	**21**	**22**	**23**	**24**	**25**	**26**	**27**	**28**	**29**	**30**	**31**	**32**	**33**	**34**	**35**	**36**
A	7.63	0.00	0.00	0.09	99.82	99.34	99.97	99.97	0.07	0.00	0.00	10.27	0.00	100.00	0.00	16.5	0.03	3.00
G	0.00	0.00	0.00	99.90	0.09	0.01	0.02	0.00	0.00	0.00	0.02	89.72	0.00	0.00	99.99	83.4	0.03	0.05
C	92.36	0.00	0.43	0.00	0.05	0.13	0.01	0.01	1.67	0.54	0.00	0.00	100.00	0.00	0.00	0.0	99.83	91.33
U	0.01	100.00	99.57	0.00	0.04	0.52	0.00	0.01	98.26	99.46	99.98	0.00	0.00	0.00	0.00	0.0	0.11	5.62
-	0.00	0.00	0.00	0.00	0.00	0.00	0.00	0.00	0.00	0.00	0.00	0.00	0.00	0.00	0.00	0.0	0.00	0.00
Pos:	**37**	**38**	**39**	**40**	**41**	**42**	**43**	**44**	**45**	**46**	**47**	**48**	**49**	**50**	**51**	**52**	**53**	**54**
A	0.00	99.94	0.00	0.00	99.99	3.01	99.98	99.86	70.23	1.52	0.00	53.78	99.98	0.01	0.00	0.0	0.00	76.95
G	0.00	0.00	0.00	0.00	0.00	96.95	0.01	0.11	25.19	0.00	99.99	46.12	0.00	0.02	99.99	100.	100.00	22.11
C	0.02	0.00	72.36	100.00	0.00	0.03	0.01	0.03	4.53	98.47	0.01	0.04	0.02	0.00	0.00	0.0	0.00	0.07
U	99.98	0.06	27.64	0.00	0.00	0.00	0.00	0.00	0.04	0.01	0.00	0.07	0.00	99.97	0.01	0.0	0.00	0.86
-	0.00	0.00	0.00	0.00	0.00	0.00	0.00	0.00	0.00	0.00	0.00	0.00	0.00	0.00	0.00	0.0	0.00	0.00
Pos:	**55**	**56**	**57**	**58**	**59**	**60**	**61**	**62**	**63**									
A	0.15	0.00	0.47	0.00	100.00	38.94	94.85	0.00	3.22									
G	98.78	0.02	99.47	0.00	0.00	61.04	0.09	0.00	96.72									
C	0.02	0.01	0.02	100.00	0.00	0.01	5.00	0.01	0.01									
U	1.05	99.97	0.04	0.00	0.00	0.01	0.06	99.99	0.05									
-	0.00	0.00	0.00	0.00	0.00	0.00	0.00	0.00	0.00									

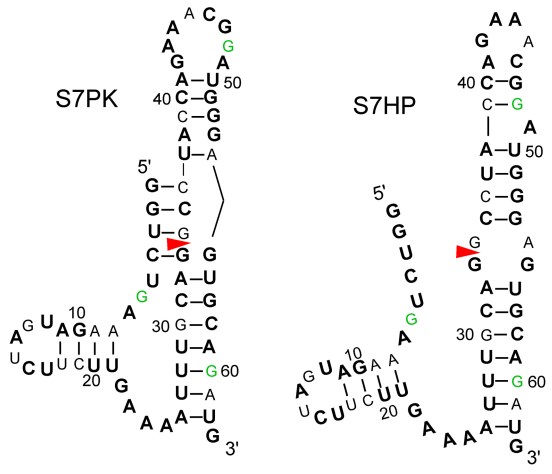

FIGURE 2. Graphic presentation of data in Tables 1 and 2. With the exception of G48, nucleotides represented as bold black, regular black, or green, have cut off fractions of a shown base of >0.965, >0.70, and >0.50, respectively (Table 2). A or G not bolded usually have a minor fraction of G or A (Table 2). C or U not bolded usually have a minor fraction of U or C (Table 2). Nucleotide 48 is 54% A and 46% G. It is represented as G because the 39–48 bp in S7HP has fractional occurrences of 0.41 CG, 0.31 CA, 0.23 UA, and 0.05 UG (Table 1). Moreover, G has been used in model hairpins (Fig. 1) to increase oligonucleotide binding and provide possible formation of a G48A43 pair in S7PK in HP1. On the basis of nucleotide fractions in Table 2, G22A7, G42A49, and/or G63A25 pairs could cap helixes. Such GA caps are prevalent in known RNA secondary structures (Elgavish et al. 2001). Terminal GA nearest neighbors are also thermodynamically stable (Sugimoto et al. 1987).

very similar (Fig. 6A; Supplemental Tables S1, S2). The average chemical shift deviation between HP2-PK and HP1 residues 5–14 is 0.010 ppm ($|\Delta\delta|_{avg}$ of H1′, H6/8, and H2/5). Chemical shifts (Supplemental Table S2) also indicate the 3D structures of HP2-HP and the 5′-CAGAAACG hairpin loop (Chen et al. 2015) of S7HP (Figs. 1B, 2) are similar. Between HP2-HP residues 4–11 and the 5′CAGAAACG hairpin loop of S7HP (Chen et al. 2015), the average deviation is 0.02 ppm (Fig. 6B). In contrast, chemical shifts between equivalent residues of the hairpin loop of HP2-PK and the 5′AGAAAC hairpin loop of S7HP (Chen et al. 2015) and between equivalent residues of HP2-HP and HP1 differ by 0.13 ppm and 0.24 ppm, respectively (Fig. 6).

On the basis of chemical shift similarities, the 5′AUC/3′UAG base-pairings in the stems of HP2-PK and HP2-HP have similar 3D structures even though the loops are different ($|\Delta\delta|_{avg}$ is 0.064 ppm) (Supplemental Table S2). Evidently, the slippage of base-pairing retains the same 3D shape of the helix because sequences of the first four stem base pairs are the same even though the pairing partners on the 3′ side change (Fig. 1C). Further evidence of slippage comes from NOE data for HP2-HP showing a cross-peak between A1H2 and G15H1′, but no detectable cross-peak between A1H2 and A19H1′. Conversely, for HP2-PK there is a medium NOE cross-peak between A1H2 and A19H1′. Overlaps in HP2-PK, however, prevent assessment of a potential cross-peak between A1H2 and G15H1′.

Two copies of 5′GGA in the natural S7PK/S7HP sequence (Fig. 1A) allow the slippage observed between HP2-PK and HP2-HP (Fig. 1C). In S7PK, the G51–C40 pair is present in 100% of sequences, and G52 forms a CG or UG pair with nucleotide 39 in 72% and 28% of sequences, respectively (Table 1). For S7HP, G47 forms a CG pair with C40 in 100% of sequences, and nucleotide 48 can form a canonical pair with nucleotide 39% in 69% of sequences. The remaining 31% of sequences can have a C39–A48 pair (Table 1). The sequence variation of nucleotides 39 and 48 suggests there may be an interesting and variable 3D structure adjacent to the S7HP hairpin loop.

The IAV segment 7 splice site is restrained as part of two canonical pairs when in the S7PK pseudoknot (Fig 1A). In contrast, the splice site is in a dynamic internal loop (Chen et al. 2015) when part of the S7HP secondary structure (Fig. 1A). This difference suggests that splicing could be inhibited with compounds stabilizing the hairpin loop of HP2-PK relative to that of HP2-HP. Reducing splicing can decrease virus viability (Jiang et al. 2016). HP2 mimics the equilibrium of a hairpin that rearranges by sliding 3 bp between the S7PK and S7HP conformations (Fig. 1A,C). Thus, HP2 could serve as a target for screening compounds able to test this model and potentially provide lead compounds for therapeutics.

Oligonucleotides targeted to HP2-PK shift the equilibrium of HP2

Titrations monitored with 1D imino proton NMR spectra were used to test whether the binding of short oligonucleotides will shift the equilibrium of HP2. Three oligonucleotides (green in Fig. 1D) were used for these experiments: 5′$U^m(_{5m}C^L)C^mG^LU^m$ (Oligo 1), 5′$C^m(_{5m}C^L)G^m(T^L)U^m$ (Oligo 2), and 5′$C^m(_{5m}C^L)G^m(T^L)U^mU^m$ (Oligo 3). Here, superscripts m and L, respectively, following a nucleotide denote 2′O-methyl and LNA sugars; $_{5m}C^L$ denotes a 5-methyl C LNA.

At 20°C, each oligonucleotide binds to 0.50 mM HP2 in a 1:1 stoichiometry (Fig. 7). Assignment of imino protons in the NMR spectrum of the HP2:Oligo1 complex (Fig. 3C) were made by connection of Watson–Crick pairs (Fig. 8) to the backbone walk in 2D NOESY spectra. Pairs identified in the stem (A1–U18, U2–A17, C3–G16, C4–G15, and A5–U14) indicate that Oligo1 shifted the HP2 equilibrium completely to HP2-PK. This is further supported by long-range NOEs such as A1H2–A19H1′, A17H2–C3H1′, and A5H2–G15H1′ that would be absent if binding was only to HP2-HP (Supplemental Table S4). NOEs expected if binding was partially to HP2-HP are not observed. Moreover, chemical shifts of U2H3 and U18H3 are unchanged in HP2:Oligo1 relative to their shifts in HP2-PK,

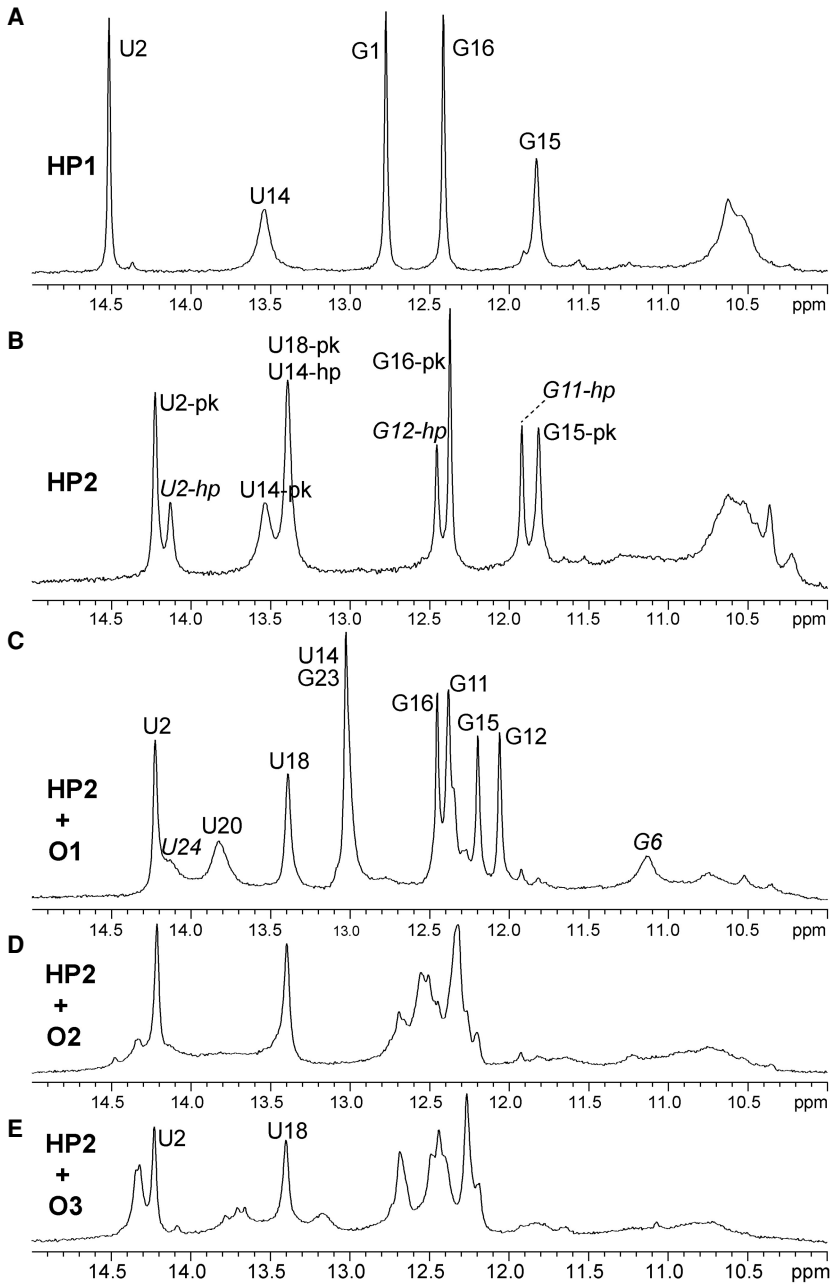

FIGURE 3. 1D imino proton spectra at 1°C of 1.5 mM HP1 (*A*), 0.5 mM HP2 (*B*), 0.5 mM HP2 + Oligo1 (*C*), 0.5 mM HP2 + Oligo2 (*D*), and 0.5 mM HP2 + Oligo3 (*E*). Sharp peak at 10.35 ppm in *B* is likely due to G6 in GAAA tetraloop of HP2-HP (Chen et al. 2015). Buffers are 0.05 mM Na_2EDTA (pH 6.2) with 2 mM potassium phosphate for HP1 and 10 mM potassium phosphate for solutions with HP2.

consistent with being furthest from the site of oligonucleotide binding. One-dimensional imino proton spectra of HP2 complexed with Oligo2 or Oligo3 (Fig. 3D,E, respectively) contain peaks at these same two spectral positions (14.2 and 13.4 ppm). Assignment of these two peaks to pairs U2–A17 and U18–A1 were confirmed with 2D NOESY spectra of HP2:Oligo3. These observations suggest that Oligo2 and Oligo3 also shift the equilibrium completely to HP2-PK.

The titrations at 20°C in Figure 7 show continuous reduction to minimal area for resonances near 12 ppm upon addition of oligonucleotides to roughly the same concentration as HP2. This is consistent with 1:1 stoichiometry of binding and $K_d < 0.5$ mM in 10 mM potassium phosphate (pH 6.2). Presumably, K_d would be tighter at a higher salt concentration. Measurements at higher salt would require designing a construct able to form hairpin but not duplex, for example, by covalently connecting the 5′ and 3′ termini.

Oligo1 forms at least 4 bp with the loop of HP2-PK

The HP2:Oligo1 complex (Fig. 1D) was further studied by NMR. Spectra confirmed that Oligo1 forms four Watson–Crick pairs with C10 to A13 and that the HP2-PK stem base pairs are stable (Figs, 3C, 8). A peak at 14.13 ppm in the 1D spectrum yields no 2D NOESY cross-peaks to identify it, but this chemical shift is typical of U imino protons in Watson–Crick pairs. It is likely that this peak is due to U^m24 of Oligo1 forming a pair with A9. A very small NOESY cross-peak between A9H2 and U^m24H1′ provides further support for the presence of this pair. It is possible the A9–U^m24 pair forms only transiently.

The A13–U^m20 pair at the 5′ end of Oligo1 may also be less stable than others as evidenced by the broad U^m20H3 resonance (Fig. 3C) and missing assignments for U^m20H5 and H6 (Supplemental Table S3). Nevertheless, the formation of the HP2-PK:Oligo1 complex rigidifies most of the HP2-PK loop nucleotides. In particular, the J(H1′–H2′) couplings of residues 8 through 12 disappear, indicating the ribose groups are held in C3′-endo conformation. Further, G11 and G12 no longer display partial syn character. In general, the base pair helix between HP2 and Oligo1 is rigid. In contrast, on the other side of the loop, G6 and A7 exhibit dynamic behavior with J (H1′–H2′) couplings of ∼3 and 2.5 Hz, respectively, and slight *syn* character of G6 suggested by H8–H1′ distance of 3.15 Å (Supplemental Table S4).

TABLE 3. Comparison between NMR results for HP1 (Fig. 1B), 5′GUCCAGAAACGGAUGGACA, and the duplex (Fig. 1E), DUP, $(5'CCAGAAACGGAUGGA)_2$

HP1/DUP Residues	NOEs Atoms	HP1/DUP Å
A7–A13/A5–A11*	H2–H1′	3.7/3.0
A13–A7/A11*–A5	H2–H1′	3.7/3.0
A8–G11/A6–G9*	H2–H2′	3.2/>5.0
A8–G12/A6–G10*	H2–H1′	4.1/>5.0
G11–G11/G9–G9	H8–H1′	2.9/4.0
G12–G12/G10–G10	H8–H1′	2.8/4.0
G6–G6/G4–G4	H8–H1′	3.3/4.4

HP1/DUP	Chemical shifts		HP1/DUP
Residue	Atom	Avg, ppm	ppm
A13/A11	P	−4.0 ± 0.4	−2.6/+0.2
U14/U12	H1′	5.6 ± 0.25	4.9/4.0
G11/G9	H2′	4.5 ± 0.23	4.6/3.4
G11/G9	C8	137.1 ± 1.0	139.8/137.2
G12/G10	C8		140.1/——

As shown in Figure 1E, asterisks (*) indicate equivalent in the duplex. Average chemical shifts include all residues in HP1 and duplex other than those listed individually.

3D modeling of the HP2:Oligo1 complex and similarities to GAAA tetraloops

Restraints derived from NMR data were used to model the HP2:Oligo1 complex. A representative model from the resulting ensemble is shown in Figure 9. A Watson–Crick pair between A9 and U^m24 was assumed, based on assignment of the imino proton peak at 14.13 ppm as U^m24. Positions of residues G6 and A7 are highly variable near the major groove of the base pairs formed with Oligo1. In particular, G6 is found in at least three different hydrogen-bonded arrangements with three different bases, or extruded near the oligonucleotide backbone. Some of the extruded G6 conformations include a *syn* G6. The backbone makes a sharp turn between A7 and A8, consistent with the A8P chemical shift that is different from the other residues (−2.7 ppm vs. average of −3.8 ppm ± 0.2 ppm for nine unmodified, assigned residues in the complex; Supplemental Table S3). A turn between A7 and A8 is consistent with an A9–U^m24 base pair being part of a continuous 5-bp helix with the oligonucleotide shifting the turn from between A8 and G11 in the unbound loop. The shifted turn is further supported by the absence of the A8H2–G11H2′ NOE observed in the unbound loop.

The sharp turn between A7 and A8 and stacking of A8, A9, and C10 form a loop (AAAC) that is reminiscent of a GAAA tetraloop (Legault and Pardi 1994; Wu et al. 2012; Chen et al. 2015). In GAAA tetraloops, the ^{31}P chemical shift at the GA turn is also downfield relative to shifts in A-form helices, although the difference is ~2 ppm in GAAA tetraloops (Legault and Pardi 1994; Chen et al. 2015) but ~1 ppm in the HP2:Oligo1 complex. This could be due to a dynamic A7 as suggested above. Stacking of A8, A9, and C10 is similar to that of AAA in GAAA tetraloops. That stacking is largely retained even in simulations with A9–U^m24 hydrogen-bond restraints removed and U^m24 extruded.

Two MD simulations of HP2:Oligo1 at 298 K were carried out for 0.5 µsec each in explicit solvent without restraints in an attempt to identify stable or transient conformations that might be hidden by NMR restraints that represent the average of multiple conformations. Two starting structures were selected from the restrained calculations described above. The short simulations suggest the C10 G11 G12 A13 / U^m20 $_{5m}C^L21$ C^m22 G^L23 base pairs in Figure 1D are stable, but the A9–U^m24 *cis* Watson–Crick/Watson–Crick pair is transitory. It was present only in 47% of frames. Occurrences of U^m24 in other base pairs include A8–U^m24 in a *cis* WC/Hoogsteen pair (24%), A9–U^m24 in a *trans* WC/Hoogsteen pair (16%), and A8–U^m24 rarely in a *cis* WC/WC pair. Unlike the A9–U^m24 *cis* WC/WC pair, none of these alternate base pairs satisfy all the NOE restraints. They may occur, but they cannot be dominant conformations. Residues A8, A9, and U^m24 are in various extruded or otherwise unpaired conformations in 11% of the frames.

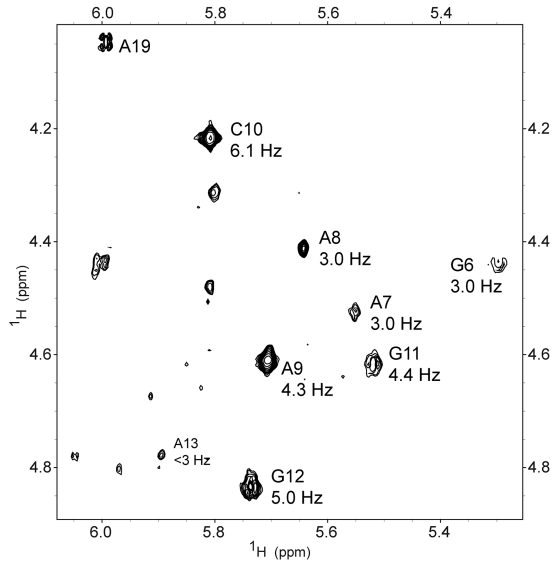

FIGURE 4. NMR 2D TOCSY spectrum of 3 mM HP1 at 25°C with mixing time of 29 msec in D_2O. H1′–H2′ cross-peaks are labeled with corresponding residue. The magnitude of the H1′–H2′ scalar-coupling constant (^3J) determined from splitting of H1′ peaks in a 400 msec mixing time NOESY spectrum is given *below* the residue identifier. Coupling accuracy is approximately ±0.5 Hz.

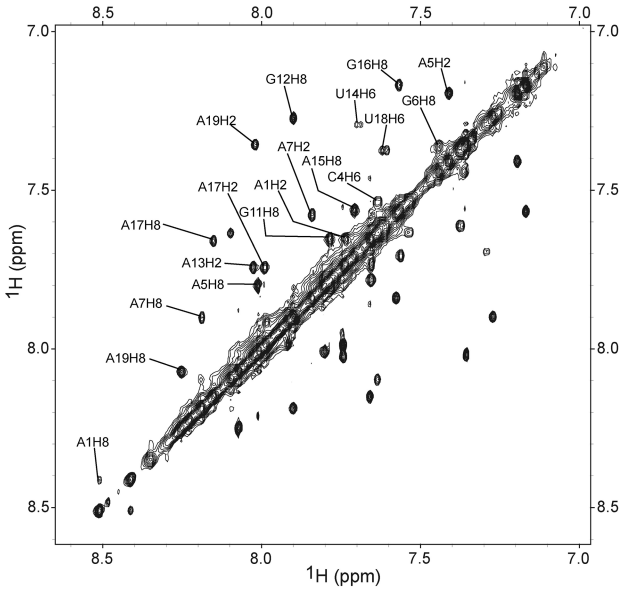

FIGURE 5. Aromatic region near the diagonal of a 2D TOCSY spectrum of 2.0 mM HP2 showing direct exchange cross-peaks between two conformations, HP2-PK and HP2-HP. Temperature is 20°C and mixing time is 29 msec. Assignment of each chemical shift to HP2-PK or HP2-HP is available in Supplemental Table S2.

In unrestrained simulations, G6 and A7 primarily remain stacked together, but oriented perpendicular to other bases in the duplexed strands, much as in the NMR restrained models. The position of A7, however, is significantly different between unrestrained and restrained simulations. NOE cross-peaks between A7 and C10 (A7H2–C10H5, A7H2–C10 amino, A7H1′–C10 amino) indicate A7 and C10 bases are in close proximity. In contrast, unrestrained simulations exhibit a large population of conformations where A7 does not interact with the helix formed by Oligo1. Nonetheless, the unrestrained simulations predict that the NOE-derived distance for A7H2 to C10H5, for instance, is 4.0 Å, which is within the maximum allowed distance of 4.5 Å in the NMR-restrained calculation. The possibility of a large population of extra-helical A7 residues cannot be excluded.

DISCUSSION

RNAs are increasingly becoming targets for therapeutics (Dominski and Kole 1993; Goemans et al. 2011; Voit et al. 2014; Disney and Angelbello 2016; Angelbello et al. 2018; Warner et al. 2018; Meyer et al. 2020) and splice sites are particularly promising targets (Dominski and Kole 1993; Garcia-Blanco et al. 2004; Douglas and Wood 2011; Kole et al. 2012; Singh and Cooper 2012; Pao et al. 2014). Discovery that a splice site in IAV is encased in a sequence that can be in equilibrium between a pseudoknot and a long hairpin (Figs. 1A, 2) suggests that perturbation of that equilibrium could be a therapeutic strategy. The pseudoknot structure sequesters the splice site in a canonical helix, presumably inhibiting splicing. In contrast, the hairpin structure exposes the splice site in a dynamic 2 × 2-nt internal loop (Moss et al. 2011, 2012; Chen et al. 2015). A key difference between the pseudoknot and long hairpin is folding of the red and blue sequences at the top of Figure 1A. The model HP2 sequence (Fig. 1C) studied here reproduces the equilibrium for that part of the natural sequence. Thus, it provides a model system that can be used to screen for molecules able to perturb the equilibrium between pseudoknot and long hairpin.

Oligonucleotides provide a relatively easy way to predict compositions able to bind RNA because rules for Watson–Crick pairing (Watson and Crick 1953) and for estimating thermodynamic stability of RNA complexes are known (Xia et al. 1998; Kierzek et al. 2005, 2006; Chen et al. 2012). These simple design principles provide a rapid approach to overcome resistance due to natural sequence mutations. Moreover, when regulation requires slippage of several base pairs as in Figures 1A and 2, evolution of resistance may take longer because concerted mutations are required. NMR spectra presented here confirm the ease of design for perturbing an RNA equilibrium. All three oligonucleotides shift the equilibrium to a single secondary structure (Fig. 3C–E). Imino proton NMR spectra of 5′$U^{m}(_{5m}C^{L})C^{m}(G^{L})U^{m}$ bound to HP2 indicate that at least 4 and probably 5 bp contribute to the binding. NMR restrained 3D models (Fig. 9) and unrestrained MD

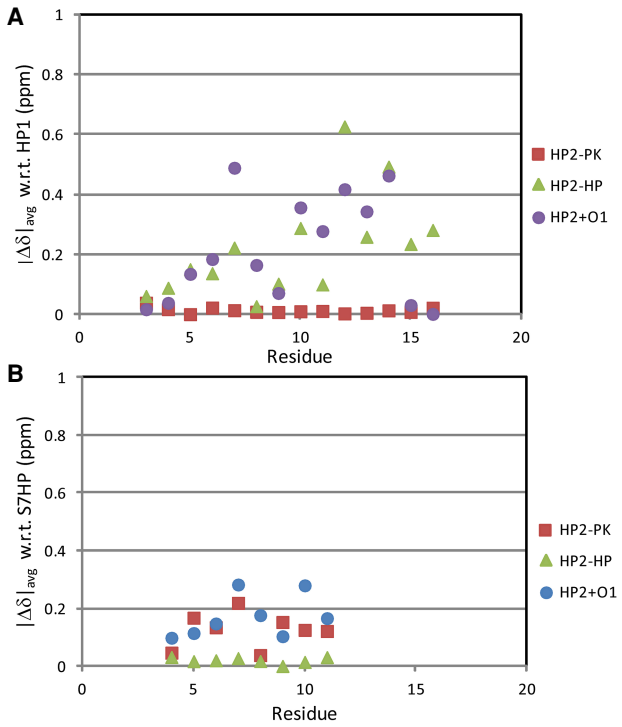

FIGURE 6. Average of absolute values of H1′, H8/6, and H2/5 chemical shift differences ($|\Delta\delta|_{avg}$) of HP2-PK, HP2-HP, and HP2 + Oligo1 compared with HP1 (*A*) and S7HP (*B*) (Chen et al. 2015).

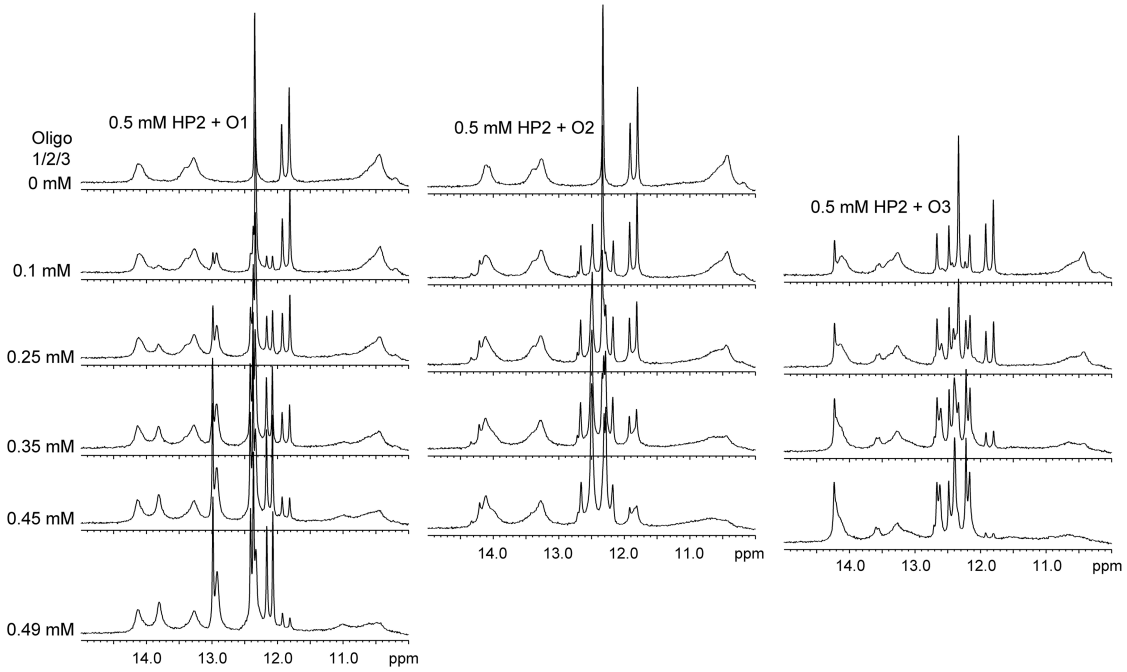

FIGURE 7. NMR spectra of imino protons in 0.5 mM HP2 (10 mM potassium phosphate, 0.05 mM Na_2EDTA at pH 6.2) with indicated additions of Oligo1 (O1), Oligo2 (O2), or Oligo3 (O3) at 20°C.

simulations support this base-pairing model. The NMR-derived models suggest that while 3 of the 8 nt in the loop of HP2:Oligo1 are not involved in pairs (Fig. 1D), A8 is well positioned to form a pair if an additional residue were present at the 3′ end of Oligo1. Thus, it appears that just two unpaired nucleotides in the loop are enough to accommodate the junction between stem and loop/oligo duplex.

Currently, FDA–approved oligonucleotides targeting mRNA are relatively long, typically containing >15 nt (Pao et al. 2014) and as many as 42 nt (Hoy 2018; Dhuri et al. 2020). They often rely on cleavage of an mRNA (Crooke et al. 2018). Such long oligonucleotides run the risk of lacking specificity due to binding strongly to sequences that are not perfect matches (Herschlag 1991). In principle, shorter oligonucleotide therapeutics could act by directing misfolding to an inactive structure (Childs et al. 2002, 2003). With that strategy, specificity can be achieved because it depends on the structure and function of the target in addition to sequence. For example, in vitro splicing can be inhibited with an 8-mer oligonucleotide that directs misfolding of a pseudoknot containing a splice site (Childs et al. 2002). The results presented here suggest that in some cases an opposite strategy of stabilizing a correctly folded intermediate structure may also be viable and that a short oligonucleotide may be sufficient. Short oligonucleotides also offer advantages in ease of design, testing of modifications, and cost of synthesis.

NMR titrations presented in Figure 7 indicate that almost complete binding is achieved at 20°C when both RNA hairpin and $5'U^m(_{5m}C^L)C^m(G^L)U^m$ are at 0.5 mM. Additional modifications can further enhance binding of short oligonucleotides to RNA. For example, replacing a U–A pair inside a helix with a pseudoU–A pair can increase stability by 0.3–2.7 kcal/mol at 37°C (Hudson et al. 2013; Kierzek et al. 2014).

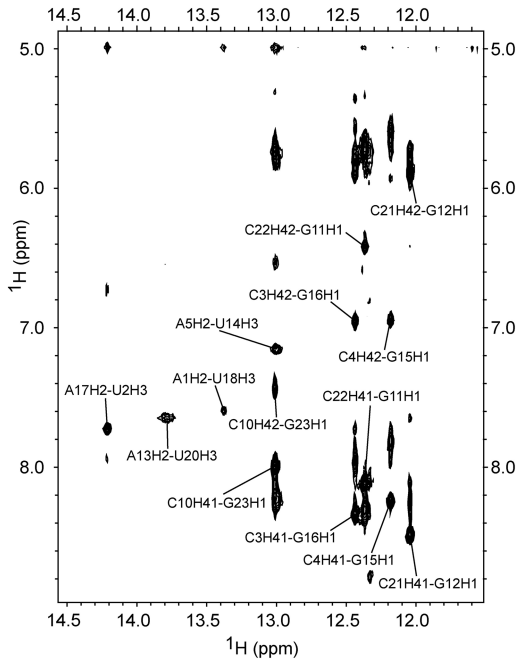

FIGURE 8. NMR 2D NOESY spectrum of 0.5 mM HP2:Oligo1 in 10 mM potassium phosphate and 0.05 mM Na_2EDTA (pH 6.2) with mixing time of 150 msec at 1°C in 95% H_2O/5% D_2O.

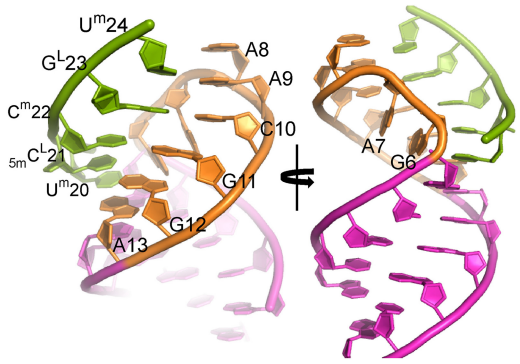

FIGURE 9. Representative NMR model of HP2:Oligo1. Views include HP2 stem (magenta; residues 1–5 and 14–19), loop (amber; residues 6–13), and Oligo1 (green; residues 20–24).

Moreover, N1-methylpseudoU can increase cellular lifetime of RNA (Mauger et al. 2019). Modification by propynylation at C5 of pyrimidines enhances binding of DNA to DNA and to RNA (Wagner et al. 1996; Barnes and Turner 2001a,b; He and Seela 2002). In principle, the oligonucleotide could be extended to allow formation of base triples with the hairpin stem (Gupta et al. 2012; Zengeya et al. 2012; Ong et al. 2019). Thus, the structural data identify a model system for screening or designing small compounds that could affect splicing in IAV and also suggest that short, modified oligonucleotides are one possible modality. Other modalities can also specifically bind RNA loops (Shortridge and Varani 2015; Disney 2019) with binding constants required for therapeutics. For high-throughput screening at low concentration of RNA where duplex would not form, HP2 could be modified by adding a fluorophore and quencher FRET pair (Forster 1949; Stryer and Haugland 1967; Clegg 1992; Roy et al. 2008) at the 5′ and 3′ ends. Stabilization of the 8-nt hairpin loop relative to the 6-nt hairpin loop (Fig. 1) would then be detected by reduced fluorescence upon addition of a binder. This would allow measurements at 37°C and physiological salt concentrations. It is also likely that similar approaches could be applied to other RNA switches, especially ones requiring unfolding of a pseudoknot.

MATERIALS AND METHODS

Oligonucleotide synthesis

Desalted and 2′ deprotected RNA hairpins, HP1 (5′ GUCCA GAAACGGAUGGACA 3′) and HP2 (5′ AUCCAGAAACGGAUG GAUA 3′), were ordered from Dharmacon on a 5.0 µmol scale. No additional purification was necessary before suspending them in buffers for NMR.

Modified oligonucleotides were synthesized on a BioAutomation MerMade12 DNA/RNA synthesizer using β-cyanoethyl phosphoramidite chemistry and commercially available phosphoramidites (ChemGenes, GenePharma). For deprotection, oligoribonucleotides were treated with a mixture of 30% aqueous ammonia for 16 h at 55°C. Deprotected oligonucleotides were purified by silica gel thin-layer chromatography (TLC) in 1-propanol/aqueous ammonia/water (55/35/10 [v/v/v]) as described previously (Kierzek and Kierzek 2003).

NMR spectroscopy and assignment

Buffers for NMR samples were 2.0 mM (HP1) or 10 mM (HP2) potassium phosphate and 0.05 mM Na_2EDTA (pH 6.2). Spectra were collected with a Varian Inova 600 MHz spectrometer. One-dimensional imino proton spectra were collected at 1°C and 20°C using a 1-1-spin-echo water suppression pulse (Sklenar and Bax 1987). Two-dimensional (2D) NOESY spectra in 95% H_2O/5% D_2O were collected using a WATERGATE pulse (Piotto et al. 1992; Grzesiek and Bax 1993) with flipback for water suppression at 1°C and 20°C and mixing times of 100 and 400 msec.

One-dimensional spectra of nonexchangeable protons were collected in D_2O at 20°C. Assignment of nonexchangeable protons was achieved with 2D NOESY (75-, 175-, and 400-msec mixing times, except HP1 with just 175 and 400 msec), TOCSY (32-msec mixing time), natural abundance ^{13}C–^{1}H sensitivity enhanced HSQC, and ^{31}P–^{1}H HETCOR spectra.

Spectra from 2D NMR were processed, assigned, and integrated with NMRpipe (Delaglio et al. 1995) and NMRFAM-SPARKY (Lee et al. 2015) as described (Kauffmann et al. 2017). Imino proton assignments were made by cross-peaks to cytosine H5 and H6 for GC pairs and to adenine H2 for AU pairs.

Restraint generation

Distances between nonexchangeable protons were obtained from spectra at 20°C and 75 msec (HP2:Oligo1) or 175 msec (HP1) mixing time as similarly reported (Kauffmann et al. 2017). NOE cross-peak volumes were $(1/r)^6$ scaled assuming 2.71 Å for H1′–H2′ cross-peak volumes of A1, G15, and U18 and 3.2 Å for H1′–H4′ of A1 and G15. Upper and lower bounds for distance restraints were calculated allowing a fourfold error in NOE volume measurements. For exchangeable protons, lower bounds were set to 2.0 Å, and upper bounds were set to 4.5, 5.0, or 6.0 Å, respectively, for large, medium, or small NOE volumes. Hydrogen bond restraints were applied between bases where NOEs indicated *cis* Watson–Crick base pairs.

Dihedral angles for Watson–Crick stems were restrained to typical A-form values, as described (Kauffmann et al. 2017). Based on the size of intraresidue H8/H6–H1′ NOE cross-peaks being consistent with χ in an *anti* conformation, χ was restrained to −255° ± 85° in all residues except G11 and G12 in HP1, and G6 in HP2:Oligo1. In the loop of HP1, no other dihedral angles were restrained. In HP2:Oligo1, ribose puckers for G6, A7, and A8 were not restrained. All other residues were restrained to C3′-endo, δ (80° ± 35°). Other than χ and δ, no dihedral angles were restrained in the loop or oligo of HP2:Oligo1.

Structure generation

Structures were generated as described (Kauffmann et al. 2017), but using AMBER 16 (Case et al. 2016) with restrained simulated

annealing starting with a structure generated from NUCGEN (Bansal et al. 1995). Coordinates, restraints, and chemical shifts are deposited with the Protein Data Bank (ID# 7RQ5) and BMRB (ID# 30940). A generalized Born implicit solvent was used with a salt concentration of 0.1 M NaCl (Still et al. 1990). Limited restrained simulations at lower salt gave essentially identical results.

MD simulations

Unrestrained simulations of HP2:Oligo1 were carried out in TIP3P solvent using AMBER 16. Force field parameters for LNA nucleotides were taken from Condon et al. (2014), with 5-methyl charge and angle parameters in $_{5m}C^{L}$ adjusted to match replaced H5 in C^{L}. Charges in 2′O-methyl modifications were adjusted to match replaced 2′-OH charges; angle and torsion parameters were taken from the AMBER library. Two starting structures were selected from an ensemble of 50 NMR structures generated with NMR restraints.

Structures were immersed in a truncated octahedral box filled with TIP3P water (Jorgensen et al. 1983) such that there was at least 10 Å of water from all surfaces of the complex. Enough Na^+ ions were added to neutralize the RNA charge, resulting in ∼0.1 M Na^+ concentration, which is higher than the bulk Na^+ concentration used for the NMR experiments. Systems were then energy minimized in two stages. First, the RNA was held fixed and only water molecules were minimized for 1000 steps of 2 fsec each. Second, the whole system was allowed to equilibrate for 2500 steps. With the solute held fixed again, the system was heated from 0 K to 298 K over 20 psec using a Langevin thermostat (Chandrasekhar 1943) with 1 $psec^{-1}$ frequency of collision. In the final stage of equilibration, Berendsen pressure regulation (Berendsen et al. 1984) with isotropic position scaling was turned on and the system equilibrated for 1 nsec at a pressure of 1 atm. Finally, production simulations were run with Monte Carlo pressure regulation at 298 K and 1 atm (NPT ensemble). Bonds to hydrogens were constrained with the SHAKE algorithm (Ryckaert et al. 1977), which allowed 2-fsec time steps. Simulations were run with the graphical card implementation (Salomon-Ferrer et al. 2013) of the MD engine of the Amber 16 software package. All molecules were modeled with the AMBER ff99RNAOL3 force field. This force field contains the original parameters from force fields ff94 (Cornell et al. 1995) and ff99 (Cheatham et al. 1999; Wang et al. 2000) along with revisions for α and γ backbone dihedrals (Perez et al. 2007) and glycosidic dihedrals for all four bases (Zgarbova et al. 2011). Each starting structure was simulated for 0.5 μsec.

SUPPLEMENTAL MATERIAL

Supplemental material is available for this article.

ACKNOWLEDGMENTS

This research was supported by National Institutes of Health Grant R01 GM22939 to D.H.T., R01 GM133810 to W.N.M., and National Science Centre grant 2020/39/B.NZ1/03054 to E.K.

Received August 17, 2021; accepted December 13, 2021.

REFERENCES

Angelbello AJ, Chen JL, Childs-Disney JL, Zhang P, Wang ZF, Disney MD. 2018. Using genome sequence to enable the design of medicines and chemical probes. *Chem Rev* **118:** 1599–1663. doi:10.1021/acs.chemrev.7b00504

Bansal M, Bhattacharyya D, Ravi B. 1995. NUPARM and NUCGEN: software for analysis and generation of sequence dependent nucleic acid structures. *Comput Appl Biosci* **11:** 281–287. doi:10.1093/bioinformatics/11.3.281

Bao Y, Bolotov P, Dernovoy D, Kiryutin B, Zaslavsky L, Tatusova T, Ostell J, Lipman D. 2008. The influenza virus resource at the National Center for Biotechnology Information. *J Virol* **82:** 596–601. doi:10.1128/JVI.02005-07

Barnes TW III, Turner DH. 2001a. Long-range cooperativity due to C5-propynylation of oligopyrimidines enhances specific recognition by uridine of ribo-adenosine over ribo-guanosine. *J Am Chem Soc* **123:** 9186–9187. doi:10.1021/ja0157752

Barnes TW III, Turner DH. 2001b. Long-range cooperativity in molecular recognition of RNA by oligodeoxynucleotides with multiple C5-(1-propynyl) pyrimidines. *J Am Chem Soc* **123:** 4107–4118. doi:10.1021/ja003208t

Bennett CF, Krainer AR, Cleveland DW. 2019. Antisense oligonucleotide therapies for neurodegenerative diseases. *Annu Rev Neurosci* **42:** 385–406. doi:10.1146/annurev-neuro-070918-050501

Berendsen HJC, Postma JPM, Van Gunsteren WF, DiNola A, Haak JR. 1984. Molecular dynamics with coupling to an external bath. *J Chem Theory Comput* **81:** 3684–3690. doi:10.1063/1.448118

Biggerstaff M, Kniss K, Jernigan DB, Brammer L, Bresee J, Garg S, Burns E, Reed C. 2018. Systematic assessment of multiple routine and near real-time indicators to classify the severity of influenza seasons and pandemics in the United States, 2003–2004 through 2015–2016. *Am J Epidemiol* **187:** 1040–1050. doi:10.1093/aje/kwx334

Case DA, Betz RM, Cerutti DS, Cheatham I TE, Darden TA, Duke RE, Giese TJ, Gohlke H, Goetz AW, Homeyer N, et al. 2016. *AMBER 2016*. University of California, San Francisco.

Chandrasekhar S. 1943. Stochastic problems in physics and astronomy. *Rev Mod Physics* **15:** 1–89. doi:10.1103/RevModPhys.15.1

Cheatham TE III, Cieplak P, Kollman PA. 1999. A modified version of the Cornell et al. force field with improved sugar pucker phases and helical repeat. *J Biomol Struct Dyn* **16:** 845–862. doi:10.1080/07391102.1999.10508297

Chen JL, Dishler AL, Kennedy SD, Yildirim I, Liu B, Turner DH, Serra MJ. 2012. Testing the nearest neighbor model for canonical RNA base pairs: revision of GU parameters. *Biochemistry* **51:** 3508–3522. doi:10.1021/bi3002709

Chen JL, Kennedy SD, Turner DH. 2015. Structural features of a 3′ splice site in influenza A. *Biochemistry* **54:** 3269–3285. doi:10.1021/acs.biochem.5b00012

Childs JL, Disney MD, Turner DH. 2002. Oligonucleotide directed misfolding of RNA inhibits *Candida albicans* group I intron splicing. *Proc Natl Acad Sci* **99:** 11091–11096. doi:10.1073/pnas.172391199

Childs JL, Poole AW, Turner DH. 2003. Inhibition of *Escherichia coli* RNase P by oligonucleotide directed misfolding of RNA. *RNA* **9:** 1437–1445. doi:10.1261/rna.5780503

Clegg RM. 1992. Fluorescence resonance energy transfer and nucleic acids. *Methods Enzymol* **211:** 353–388. doi:10.1016/0076-6879(92)11020-J

Condon DE, Yildirim I, Kennedy SD, Mort BC, Kierzek R, Turner DH. 2014. Optimization of an AMBER force field for the artificial nucleic acid, LNA, and benchmarking with NMR of L(CAAU). *J Phys Chem B* **118:** 1216–1228. doi:10.1021/jp408909t

Cornell WD, Cieplak P, Bayly CI, Gould IR, Merz KM, Ferguson DM, Spellmeyer DC, Fox T, Caldwell JW, Kollman PA. 1995. A second generation force field for the simulation of proteins, nucleic acids,

and organic molecules. *J Am Chem Soc* **117:** 5179–5197. doi:10.1021/ja00124a002

Crooke ST, Witztum JL, Bennett CF, Baker BF. 2018. RNA-targeted therapeutics. *Cell Metab* **27:** 714–739. doi:10.1016/j.cmet.2018.03.004

Davila-Calderon J, Patwardhan NN, Chiu LY, Sugarman A, Cai Z, Penutmutchu SR, Li ML, Brewer G, Hargrove AE, Tolbert BS. 2020. IRES-targeting small molecule inhibits enterovirus 71 replication via allosteric stabilization of a ternary complex. *Nat Commun* **11:** 4775. doi:10.1038/s41467-020-18594-3

Delaglio F, Grzesiek S, Vuister GW, Zhu G, Pfeifer J, Bax A. 1995. Nmrpipe - a multidimensional spectral processing system based on Unix pipes. *J Biomol NMR* **6:** 277–293. doi:10.1007/BF00197809

Dhuri K, Bechtold C, Quijano E, Pham H, Gupta A, Vikram A, Bahal R. 2020. Antisense oligonucleotides: an emerging area in drug discovery and development. *J Clin Med* **9:** 2004. doi:10.3390/jcm9062004

Disney MD. 2019. Targeting RNA with small molecules to capture opportunities at the intersection of chemistry, biology, and medicine. *J Am Chem Soc* **141:** 6776–6790. doi:10.1021/jacs.8b13419

Disney MD, Angelbello AJ. 2016. Rational design of small molecules targeting oncogenic noncoding RNAs from sequence. *Acc Chem Res* **49:** 2698–2704. doi:10.1021/acs.accounts.6b00326

Dominski Z, Kole R. 1993. Restoration of correct splicing in thalassemic pre-mRNA by antisense oligonucleotides. *Proc Natl Acad Sci* **90:** 8673–8677. doi:10.1073/pnas.90.18.8673

Douglas AGL, Wood MJA. 2011. RNA splicing: disease and therapy. *Brief Funct Genomics* **10:** 151–164. doi:10.1093/bfgp/elr020

Elgavish T, Cannone JJ, Lee JC, Harvey SC, Gutell RR. 2001. AA.AG@helix.ends: A:A and A:G base-pairs at the ends of 16 S and 23 S rRNA helices. *J Mol Biol* **310:** 735–753. doi:10.1006/jmbi.2001.4807

Forster T. 1949. Experimental and theoretical investigation of the intermolecular transfer of electronic excitation energy. *Z Naturforsch A* **4:** 321–327. doi:10.1515/zna-1949-0501

Garcia-Blanco MA, Baraniak AP, Lasda EL. 2004. Alternative splicing in disease and therapy. *Nat Biotechnol* **22:** 535–546. doi:10.1038/nbt964

Goemans NM, Tulinius M, van den Akker JT, Burm BE, Ekhart PF, Heuvelmans N, Holling T, Janson AA, Platenburg GJ, Sipkens JA, et al. 2011. Systemic administration of PRO051 in Duchenne's muscular dystrophy. *N Engl J Med* **364:** 1513–1522. doi:10.1056/NEJMoa1011367

Grzesiek S, Bax A. 1993. The importance of not saturating water in protein NMR. Application to sensitivity enhancement and NOE measurements. *J Am Chem Soc* **115:** 12593–12594. doi:10.1021/ja00079a052

Gubareva LV, Mishin VP, Patel MC, Chesnokov A, Nguyen HT, De La Cruz J, Spencer S, Campbell AP, Sinner M, Reid H, et al. 2019. Assessing baloxavir susceptibility of influenza viruses circulating in the United States during the 2016/17 and 2017/18 seasons. *Euro Surveill* **24:** 1800666. doi:10.2807/1560-7917.ES.2019.24.3.1800666

Gultyaev AP, Heus HA, Olsthoorn RC. 2007. An RNA conformational shift in recent H5N1 influenza A viruses. *Bioinformatics* **23:** 272–276. doi:10.1093/bioinformatics/btl559

Gupta P, Muse O, Rozners E. 2012. Recognition of double-stranded RNA by guanidine-modified peptide nucleic acids. *Biochemistry* **51:** 63–73. doi:10.1021/bi201570a

Haniff HS, Tong Y, Liu X, Chen JL, Suresh BM, Andrews RJ, Peterson JM, O'Leary CA, Benhamou RI, Moss WN, et al. 2020. Targeting the SARS-CoV-2 RNA genome with small molecule binders and ribonuclease targeting chimera (RIBOTAC) degraders. *ACS Cent Sci* **6:** 1713–1721. doi:10.1021/acscentsci.0c00984

Hayden FG, Sugaya N, Hirotsu N, Lee N, de Jong MD, Hurt AC, Ishida T, Sekino H, Yamada K, Portsmouth S, et al. 2018. Baloxavir marboxil for uncomplicated influenza in adults and adolescents. *N Engl J Med* **379:** 913–923. doi:10.1056/NEJMoa1716197

He J, Seela F. 2002. Propynyl groups in duplex DNA: stability of base pairs incorporating 7-substituted 8-aza-7-deazapurines or 5-substituted pyrimidines. *Nucleic Acids Res* **30:** 5485–5496. doi:10.1093/nar/gkf689

Herschlag D. 1991. Implications of ribozyme kinetics for targeting the cleavage of specific RNA molecules in vivo: more isn't always better. *Proc Natl Acad Sci* **88:** 6921–6925. doi:10.1073/pnas.88.16.6921

Holsinger LJ, Nichani D, Pinto LH, Lamb RA. 1994. Influenza A virus M2 ion channel protein: a structure-function analysis. *J Virol* **68:** 1551–1563. doi:10.1128/jvi.68.3.1551-1563.1994

Hoy SM. 2018. Patisiran: first global approval. *Drugs* **78:** 1625–1631. doi:10.1007/s40265-018-0983-6

Hudson GA, Bloomingdale RJ, Znosko BM. 2013. Thermodynamic contribution and nearest-neighbor parameters of pseudouridine-adenosine base pairs in oligoribonucleotides. *RNA* **19:** 1474–1482. doi:10.1261/rna.039610.113

Ilyinskii PO, Schmidt T, Lukashev D, Meriin AB, Thoidis G, Frishman D, Shneider AM. 2009. Importance of mRNA secondary structural elements for the expression of influenza virus genes. *OMICS* **13:** 421–430. doi:10.1089/omi.2009.0036

Jiang T, Nogales A, Baker SF, Martinez-Sobrido L, Turner DH. 2016. Mutations designed by ensemble defect to misfold conserved RNA structures of Influenza A segments 7 and 8 affect splicing and attenuate viral replication in cell culture. *PLoS One* **11:** e0156906. doi:10.1371/journal.pone.0156906

Jorgensen WL, Chandrasekhar J, Madura JD, Impey RW, Klein ML. 1983. Comparison of simple potential functions for simulating liquid water. *J Chem Phys* **79:** 926–935. doi:10.1063/1.445869

Kauffmann AD, Kennedy SD, Zhao J, Turner DH. 2017. Nuclear magnetic resonance structure of an 8×8 nucleotide RNA internal loop flanked on each side by three Watson-Crick pairs and comparison to three-dimensional predictions. *Biochemistry* **56:** 3733–3744. doi:10.1021/acs.biochem.7b00201

Kierzek E, Kierzek R. 2003. The synthesis of oligoribonucleotides containing N^6-alkyladenosines and 2-methylthio-N^6-alkyladenosines via post-synthetic modification of precursor oligomers. *Nucleic Acids Res* **31:** 4461–4471. doi:10.1093/nar/gkg632

Kierzek E, Ciesielska A, Pasternak K, Mathews DH, Turner DH, Kierzek R. 2005. The influence of locked nucleic acid residues on the thermodynamic properties of 2′-O-methyl RNA/RNA heteroduplexes. *Nucleic Acids Res* **33:** 5082–5093. doi:10.1093/nar/gki789

Kierzek E, Mathews DH, Ciesielska A, Turner DH, Kierzek R. 2006. Nearest neighbor parameters for Watson-Crick complementary heteroduplexes formed between 2′-O-methyl RNA and RNA oligonucleotides. *Nucleic Acids Res* **34:** 3609–3614. doi:10.1093/nar/gkl232

Kierzek E, Magdalena M, Lisowiec J, Turner DH, Kierzek R. 2014. The contribution of pseudouridine to stabilities and structure of RNA. *Nucleic Acids Res* **42:** 3492–3501. doi:10.1093/nar/gkt1330

Kobayashi Y, Dadonaite B, van Doremalen N, Suzuki Y, Barclay WS, Pybus OG. 2016. Computational and molecular analysis of conserved influenza A virus RNA secondary structures involved in infectious virion production. *RNA Biol* **13:** 883–894. doi:10.1080/15476286.2016.1208331

Kole R, Krainer AR, Altman S. 2012. RNA therapeutics: beyond RNA interference and antisense oligonucleotides. *Nat Rev Drug Discov* **11:** 125–140. doi:10.1038/nrd3625

Lee W, Tonelli M, Markley JL. 2015. NMRFAMSPARKY: enhanced software for biomolecular NMR spectroscopy. *Bioinformatics* **31:** 1325–1327. doi:10.1093/bioinformatics/btu830

Legault P, Pardi A. 1994. 31P chemical shifts as a probe of structural motifs in RNA. *J Magn Reson B* **103:** 82–86. doi:10.1006/jmrb.1994.1012

Lenartowicz E, Nogales A, Kierzek E, Kierzek R, Martinez-Sobrido L, Turner DH. 2016. Antisense oligonucleotides targeting influenza A segment 8 genomic RNA inhibit viral replication. *Nucleic Acid Ther* **26:** 277–285. doi:10.1089/nat.2016.0619

Lerman YV, Kennedy SD, Shankar N, Parisien M, Major F, Turner DH. 2011. NMR structure of a 4×4 nucleotide RNA internal loop from an R2 retrotransposon: identification of a three purine-purine sheared pair motif and comparison to MC-SYM predictions. *RNA* **17:** 1664–1677. doi:10.1261/rna.2641911

Lulla V, Wandel MP, Bandyra KJ, Ulferts R, Wu M, Dendooven T, Yang X, Doyle N, Oerum S, Beale R, et al. 2021. Targeting the conserved stem loop 2 motif in the SARS-CoV-2 genome. *J Virol* **95:** e0066321. doi:10.1128/JVI.00663-21

Manning GS. 1978. The molecular theory of polyelectrolyte solutions with applications to the electrostatic properties of polynucleotides. *Q Rev Biophys* **11:** 179–246. doi:10.1017/S0033583500002031

Martin K, Helenius A. 1991. Nuclear transport of influenza virus ribonucleoproteins: the viral matrix protein (M1) promotes export and inhibits import. *Cell* **67:** 117–130. doi:10.1016/0092-8674(91)90576-K

Mathews DH. 2014. RNA secondary structure analysis using RNAstructure. *Curr Protoc Bioinformatics* **46:** 12.6.1–12.6.25. doi:10.1002/0471250953.bi1206s13

Mathews DH, Disney MD, Childs JL, Schroeder SJ, Zuker M, Turner DH. 2004. Incorporating chemical modification constraints into a dynamic programming algorithm for prediction of RNA secondary structure. *Proc Natl Acad Sci* **101:** 7287–7292. doi:10.1073/pnas.0401799101

Mauger DM, Cabral BJ, Presnyak V, Su SV, Reid DW, Goodman B, Link K, Khatwani N, Reynders J, Moore MJ, et al. 2019. mRNA structure regulates protein expression through changes in functional half-life. *Proc Natl Acad Sci* **116:** 24075–24083. doi:10.1073/pnas.1908052116

Meyer SM, Williams CC, Akahori Y, Tanaka T, Aikawa H, Tong Y, Childs-Disney JL, Disney MD. 2020. Small molecule recognition of disease-relevant RNA structures. *Chem Soc Rev* **49:** 7167–7199. doi:10.1039/D0CS00560F

Michalak P, Soszynska-Jozwiak M, Biala E, Moss WN, Kesy J, Szutkowska B, Lenartowicz E, Kierzek R, Kierzek E. 2019. Secondary structure of the segment 5 genomic RNA of influenza A virus and its application for designing antisense oligonucleotides. *Sci Rep* **9:** 3801. doi:10.1038/s41598-019-40443-7

Min JY, Subbarao K. 2010. Cellular targets for influenza drugs. *Nat Biotechnol* **28:** 239–240. doi:10.1038/nbt0310-239

Moss WN, Steitz JA. 2015. *In silico* discovery and modeling of noncoding RNA structure in viruses. *Methods* **91:** 48–56. doi:10.1016/j.ymeth.2015.06.015

Moss WN, Priore SF, Turner DH. 2011. Identification of potential conserved RNA secondary structure throughout influenza A coding regions. *RNA* **17:** 991–1011. doi:10.1261/rna.2619511

Moss WN, Dela-Moss LI, Kierzek E, Kierzek R, Priore SF, Turner DH. 2012. The 3′ splice site of influenza A segment 7 mRNA can exist in two conformations: a pseudoknot and a hairpin. *PLoS One* **7:** e38323. doi:10.1371/journal.pone.0038323

Ong AAL, Toh DK, Patil KM, Meng Z, Yuan Z, Krishna MS, Devi G, Haruehanroengra P, Lu Y, Xia K, et al. 2019. General recognition of U-G, U-A, and C-G pairs by double-stranded RNA-binding PNAs incorporated with an artificial nucleobase. *Biochemistry* **58:** 1319–1331. doi:10.1021/acs.biochem.8b01313

Pao PW, Wee KB, Yee WC, Pramono ZA. 2014. Dual masking of specific negative splicing regulatory elements resulted in maximal exon 7 inclusion of SMN2 gene. *Mol Ther* **22:** 854–861. doi:10.1038/mt.2013.276

Perez A, Marchan I, Svozil D, Sponer J, Cheatham TE III, Laughton CA, Orozco M. 2007. Refinement of the AMBER force field for nucleic acids: improving the description of α/γ conformers. *Biophys J* **92:** 3817–3829. doi:10.1529/biophysj.106.097782

Pielak RM, Chou JJ. 2011. Influenza M2 proton channels. *Biochim Biophys Acta* **1808:** 522–529. doi:10.1016/j.bbamem.2010.04.015

Pinto LH, Holsinger LJ, Lamb RA. 1992. Influenza virus M2 protein has ion channel activity. *Cell* **69:** 517–528. doi:10.1016/0092-8674(92)90452-I

Piotto M, Saudek V, Sklenar V. 1992. Gradient-tailored excitation for single-quantum NMR spectroscopy of aqueous solutions. *J Biomol NMR* **2:** 661–665. doi:10.1007/BF02192855

Putri W, Muscatello DJ, Stockwell MS, Newall AT. 2018. Economic burden of seasonal influenza in the United States. *Vaccine* **36:** 3960–3966. doi:10.1016/j.vaccine.2018.05.057

Rangan R, Watkins AM, Chacon J, Kretsch R, Kladwang W, Zheludev IN, Townley J, Rynge M, Thain G, Das R. 2021. De novo 3D models of SARS-CoV-2 RNA elements from consensus experimental secondary structures. *Nucleic Acids Res* **49:** 3092–3108. doi:10.1093/nar/gkab119

Roy R, Hohng S, Ha T. 2008. A practical guide to single-molecule FRET. *Nat Methods* **5:** 507–516. doi:10.1038/nmeth.1208

Ryckaert JP, Ciccotti G, Berendsen HJC. 1977. Numerical integration of the cartesian equations of motion of a system with constraints: molecular dynamics of n-alkanes. *J Comput Phys* **23:** 327–341. doi:10.1016/0021-9991(77)90098-5

Salomon R, Webster RG. 2009. The influenza virus enigma. *Cell* **136:** 402–410. doi:10.1016/j.cell.2009.01.029

Salomon-Ferrer R, Gotz AW, Poole D, Le Grand S, Walker RC. 2013. Routine microsecond molecular dynamics simulations with AMBER on GPUs. 2. Explicit solvent particle Mesh Ewald. *J Chem Theory Comput* **9:** 3878–3888. doi:10.1021/ct400314y

Sheu TG, Fry AM, Garten RJ, Deyde VM, Shwe T, Bullion L, Peebles PJ, Li Y, Klimov AI, Gubareva LV. 2011. Dual resistance to adamantanes and oseltamivir among seasonal influenza A (H1N1) viruses: 2008-2010. *J Infect Dis* **203:** 13–17. doi:10.1093/infdis/jiq005

Shih SR, Nemeroff ME, Krug RM. 1995. The choice of alternative 5′ splice sites in influenza virus M1 mRNA is regulated by the viral polymerase complex. *Proc Natl Acad Sci* **92:** 6324–6328. doi:10.1073/pnas.92.14.6324

Shortridge MD, Varani G. 2015. Structure based approaches for targeting non-coding RNAs with small molecules. *Curr Opin Struct Biol* **30:** 79–88. doi:10.1016/j.sbi.2015.01.008

Simon LM, Morandi E, Luganini A, Gribaudo G, Martinez-Sobrido L, Turner DH, Oliviero S, Incarnato D. 2019. *In vivo* analysis of influenza A mRNA secondary structures identifies critical regulatory motifs. *Nucleic Acids Res* **47:** 7003–7017. doi:10.1093/nar/gkz318

Singh RK, Cooper TA. 2012. Pre-mRNA splicing in disease and therapeutics. *Trends Mol Med* **18:** 472–482. doi:10.1016/j.molmed.2012.06.006

Sklenar V, Bax A. 1987. Spin-echo water suppression for the generation of pure-phase two-dimensional NMR spectra. *J Mag Res* **74:** 469–479.

Soszynska-Jozwiak M, Michalak P, Moss WN, Kierzek R, Kierzek E. 2015. A conserved secondary structural element in the coding region of the influenza A virus nucleoprotein (NP) mRNA is important for the regulation of viral proliferation. *PLoS One* **10:** e0141132. doi:10.1371/journal.pone.0141132

Sreeramulu S, Richter C, Berg H, Wirtz Martin MA, Ceylan B, Matzel T, Adam J, Altincekic N, Azzaoui K, Bains JK, et al. 2021. Exploring the druggability of conserved RNA regulatory elements in the

SARS-CoV-2 genome. *Angew Chem Int Ed Engl* **60:** 19191–19200. doi:10.1002/anie.202103693

Still WC, Tempczyk A, Hawley RC, Hendrickson T. 1990. Semianalytical treatment of solvation for molecular mechanics and dynamics. *J Am Chem Soc* **112:** 6127–6129. doi:10.1021/ja00172a038

Stryer L, Haugland RP. 1967. Energy transfer: a spectroscopic ruler. *Proc Natl Acad Sci* **58:** 719–726. doi:10.1073/pnas.58.2.719

Sugimoto N, Kierzek R, Turner DH. 1987. Sequence dependence for the energetics of terminal mismatches in ribooligonucleotides. *Biochemistry* **26:** 4559–4562. doi:10.1021/bi00388a059

Szabat M, Lorent D, Czapik T, Tomaszewska M, Kierzek E, Kierzek R. 2020. RNA secondary structure as a first step for rational design of the oligonucleotides towards inhibition of influenza A virus replication. *Pathogens* **9:** 925. doi:10.3390/pathogens9110925

Takashita E, Kawakami C, Morita H, Ogawa R, Fujisaki S, Shirakura M, Miura H, Nakamura K, Kishida N, Kuwahara T, et al. 2019. Detection of influenza A(H3N2) viruses exhibiting reduced susceptibility to the novel cap-dependent endonuclease inhibitor baloxavir in Japan, December 2018. *Euro Surveill* **24:** 1800698. doi:10.2807/1560-7917.ES.2019.24.3.1800698

Turner DH, Mathews DH. 2010. NNDB: the nearest neighbor parameter database for predicting stability of nucleic acid secondary structure. *Nucleic Acids Res* **38:** D280–D282. doi:10.1093/nar/gkp892

Voit T, Topaloglu H, Straub V, Muntoni F, Deconinck N, Campion G, De Kimpe SJ, Eagle M, Guglieri M, Hood S, et al. 2014. Safety and efficacy of drisapersen for the treatment of Duchenne muscular dystrophy (DEMAND II): an exploratory, randomised, placebo-controlled phase 2 study. *Lancet Neurol* **13:** 987–996. doi:10.1016/S1474-4422(14)70195-4

Wagner RW, Matteucci MD, Grant D, Huang T, Froehler BC. 1996. Potent and selective inhibition of gene expression by an antisense heptanucleotide. *Nat Biotechnol* **14:** 840–844. doi:10.1038/nbt0796-840

Wang J, Cieplak P, Kollman PA. 2000. How well does a restrained electrostatic potential (RESP) model perform in calculating conformational energies of organic and biological molecules? *J Comput Chem* **21:** 1049–1074. doi:10.1002/1096-987X(200009)21:12<1049::AID-JCC3>3.0.CO;2-F

Warf MB, Berglund JA. 2010. Role of RNA structure in regulating pre-mRNA splicing. *Trends Biochem Sci* **35:** 169–178. doi:10.1016/j.tibs.2009.10.004

Warner KD, Hajdin CE, Weeks KM. 2018. Principles for targeting RNA with drug-like small molecules. *Nat Rev Drug Discov* **17:** 547–558. doi:10.1038/nrd.2018.93

Watson JD, Crick FH. 1953. Molecular structure of nucleic acids; a structure for deoxyribose nucleic acid. *Nature* **171:** 737–738. doi:10.1038/171737a0

Watt AT, Swayze G, Swayze EE, Freier SM. 2020. Likelihood of non-specific activity of gapmer antisense oligonucleotides is associated with relative hybridization free energy. *Nucleic Acid Ther* **30:** 215–228. doi:10.1089/nat.2020.0847

Wu L, Chai D, Fraser ME, Zimmerly S. 2012. Structural variation and uniformity among tetraloop-receptor interactions and other loop-helix interactions in RNA crystal structures. *PLoS One* **7:** e49225. doi:10.1371/journal.pone.0049225

Xia T, SantaLucia J Jr, Burkard ME, Kierzek R, Schroeder SJ, Jiao X, Cox C, Turner DH. 1998. Thermodynamic parameters for an expanded nearest-neighbor model for formation of RNA duplexes with Watson-Crick base pairs. *Biochemistry* **37:** 14719–14735. doi:10.1021/bi9809425

Zengeya T, Gupta P, Rozners E. 2012. Triple-helical recognition of RNA using 2-aminopyridine-modified PNA at physiologically relevant conditions. *Angew Chem Int Ed Engl* **51:** 12593–12596. doi:10.1002/anie.201207925

Zgarbova M, Otyepka M, Sponer J, Mladek A, Banas P, Cheatham TE III, Jurecka P. 2011. Refinement of the Cornell et al. nucleic acids force field based on reference quantum chemical calculations of glycosidic torsion profiles. *J Chem Theory Comput* **7:** 2886–2902. doi:10.1021/ct200162x